7
High-Performance Broadband Photodetector Based on MoS_2-WS_2 Heterojunction

In this chapter, we systematically explore the light sensing performance of MoS_2 and MoS_2-WS_2 heterojunction-based photodetectors in the visible to near-infrared wavelength spectrum. First, the growth of MoS_2 flakes network via the controlled kinetics conditions of conventional chemical vapor deposition (CVD) process and crumpled WS_2 nanoparticles via hydrothermal method were explained. Subsequent to the fabrication of the MoS_2-WS_2 heterojunctions, we rigorously characterize the resultant structures to evaluate their morphological features, crystallographic integrity, electron doping characteristics, elemental composition, and optical absorption properties. As a proof of concept, we investigate the light-induced electrical responses of both pristine MoS_2 flakes and the MoS_2-WS_2 heterojunctions under illumination conditions that extend from visible to near-infrared, while concurrently assessing the responsivity, detectivity, external quantum efficiency, stability, response time, and reproducibility of the photodetectors. Our analysis underscores the promising potential of two-dimensional MoS_2 for photodetector applications, particularly via the incorporation of heterostructures such as MoS_2-WS_2, which significantly enhance photoresponse capabilities for self-powered broadband photodetection across visible to near-infrared ranges. The energy band alignment at the heterojunction interface critically affects photodetector performance, and an understanding of photo-generated carrier dynamics at the interface is crucial for high-performance devices. To gain intrinsic physical insights into device behavior and light-sensing mechanism, we analyse charge carrier dynamics using photoelectron spectroscopy (XPS) and kelvin probe force microscopy (KPFM). The demonstration of MoS_2 heterostructures as high-performance broadband photodetectors offer exciting opportunities for efficient optoelectronics and imaging applications.

7.1 Requirement of highly sensitive, fast, and broadband photodetectors

The photodetector is an important component of optoelectronics devices, which use leveraging technology to transform optical signals into electrical signals. The process involves the absorption of photons, resulting in the creation of electron-hole pairs and separation of the pair at the junction. When subjected to an electric field, they generate a current that enables the detection of the related optical signal. The next generation of multifunctional systems is experiencing a technological roadblock due to the need for broadband sensing capabilities while also reaching miniaturised footprints [Vashishtha et al., 2023; Zeng et al., 2016; Zou et al., 2022]. The demand for broadband photodetectors is now high in the field of nano-optoelectronics due to their significant contributions to a number of different applications, such as the medical field, military, optoelectronic communication, imaging, environmental monitoring, space exploration, and other related domains [Goswami et al., 2020; Kumar et al., 2021a; Lien et al., 2020; Pan et al., 2022; Pospischil et al., 2013; Xiao et al., 2019]. Broadband photodetectors (PDs) are intriguing because they can detect light from a wide range of wavelengths without the need for additional devices. This spectrum encompasses the electromagnetic spectrum's visible and near-infrared (NIR) portions. Photodetectors need to be very sensitive to light over a wide spectrum and have rapid reaction times so that they can perform these functions efficiently. A narrow photon detection bandwidth is a common consequence of the usage of many photoactive semiconductors in commercial high-performance devices with proper band alignment. In this regard, silicon, InGaAs, and GaN are used for light detection in the visible, near-infrared (NIR), and ultraviolet (UV) regimes [Aggarwal et al., 2020; Ejeckam et al., 1995; Gundimeda et al., 2017; Ye et al., 2013].

Transition metal dichalcogenides (TMDs) have been the subject of intense research in recent years due to their unique semiconductor features, including the small band gap and high

carrier mobility, as compared to 3D semiconductors like silicon and germanium [Huang et al., 2006; Jariwala et al., 2014; Vivien et al., 2009]. However, the task of assuring certain attributes, such as flexibility, is a persistent challenge for devices based on 3D semiconductors. The optoelectronic properties of two-dimensional (2D) transition metal dichalcogenides (TMDCs) have garnered significant attention in research due to their large surface-to-volume ratio feature with excellent photoresponsivity, detectivity, external quantum efficiency, flexibility, and spectral response range capabilities [Lee et al., 2013; Lopez-Sanchez et al., 2013; Wang et al., 2012; Xie et al., 2017b]. Molybdenum disulfide (MoS_2) is one of the most extensively studied and leading 2D semiconductors, have garnered attention as a potential next-generation broadband photodetector (PD) due to its direct and adjustable bandgap, large current on/off ratio, high carrier mobility and a high absorption coefficient, among other interesting properties [Feng et al., 2021; Jariwala et al., 2014; Jiang et al., 2020]. MoS_2 is a popular layered transition metal dichalcogenide consisting of a stack of planes in which S-Mo-S atoms in each layer are covalently bound to one another in a hexagonal structure and each of the adjacent planes are kept connected through van der Waals interactions. As compared to the most prevalent sunlight absorbers Si and GaAs, MoS_2 has one order of magnitude higher sunlight absorption [Bernardi et al., 2013].

Considering the significant advancements in the performance of MoS_2 photodetectors, using a single material constrains the performance of photodetectors due to the low absorption of light. So, the performance of the photodetector may be significantly improved by integrating two or more high-absorbing materials to obtain outstanding light absorption and broad-spectrum response [Long et al., 2016b; Wadhwa et al., 2021b; Yu et al., 2013]. As a result, MoS_2 optical absorption may be increased by developing a heterostructure with other materials having high optical absorption. Heterostructure photodetector devices have a better photo response and can enable more functionality ability than single-material devices [Yang et al., 2017b]. Since 2D materials have several unique physical properties, including dangling-bond-free surfaces, which make it possible to produce heterostructures without any mismatches in the atomic lattice [Zhang et al., 2020b]. The fabrication of 2D material heterostructures yields atomically thin surfaces and novel optoelectronic features, allowing for room-temperature photodetection and providing a distinctive material framework for basic research. In recent years, a plethora of 2D material heterostructure-based photodetectors have been developed including graphene/MoS_2 [Thai et al., n.d.], WSe_2/MoS_2 [Shin et al., 2020], and MoS_2/black phosphorus [Bullock et al., 2018]. Despite the excellent physical properties, MoS_2/WS_2 heterostructures have seen relatively little research into optoelectronic applications. In a previous study, Wu, W. *et al*., successfully fabricated monolayer MoS_2-WS_2 in-plane heterostructures. These heterostructures demonstrated a spectrum responsivity (R_λ) of 4.36 mA/W and a detectivity (D*) of 4.36×10^{13} Jones when subjected to an optical power density of 28.64 mW/cm^2 at a wavelength of 532 nm [Wu et al., 2018b]. Xin *et al*. present a polarization-sensitive based self-powered GeSe/MoS_2 p-n heterojunction photodetector. When illuminated by a 532 nm laser at zero bias, the self-powered photocurrent displays an impressive on-off ratio of over 10^4, in addition to a high responsivity of 105 mA/W, a detectivity of 1.03×10^{10} Jones, and an EQE of 24.2%, and a rapid photo response speed (rise time = 110 ms and decay time = 750 ms) [Xin et al., 2020]. Furthermore, the similar crystal structures of MoS_2 and WS_2, two examples of 2D layered materials, allow for the development of tailored heterojunctions without the significant constraint of lattice match seen in traditional semiconductor heterostructures [Samad et al., 2016].

7.2 Device fabrication from MoS_2-WS_2 heterojunction and light-sensing experimental details

Large-area MoS_2 flake networks were synthesized using a thermal chemical vapor deposition (CVD) method with MoO_3 and sulfur as precursors. During the process, the MoO_3 source was heated to 850°C, while the sulfur source was maintained at 200°C. Argon gas was used as the carrier at a flow rate of 80 SCCM under atmospheric pressure for 45 minutes. The synthesis procedure is described in detail in Chapter 3. WS_2 nanoparticles, on the other hand, were

prepared through a hydrothermal synthesis method. The complete fabrication process for the WS_2/MoS_2 heterojunction-based photodetector device, along with its characterization, has also been elaborated in Chapter 3 under the device fabrication setps.

7.3 Characterization of MoS_2-WS_2 heterojunctions

FE-SEM micrographs were used to investigate the continuity and surface morphology of the grown MoS_2 film and MoS_2-WS_2 heterostructure. Figure 7.1 (a), displays FE-SEM images of pristine MoS_2 nanosheet grown using CVD and functionalized WS_2 on the surface of MoS_2 at various locations of the samples. It can be seen that nearly all of the WS_2 NPs are coated over the edges of the MoS_2 flakes, and a few of the WS_2 NPs are anchored over the edges of the MoS_2 flakes, with some of the WS_2 NPs diffuse into MoS_2 nanosheets. As the surface area of MoS_2 flakes is very large [He et al., 2019], the decorated WS_2 will generate a large area of contact, which is highly suggested for adequate carrier movement at the interface. Elemental mapping via energy dispersive spectroscopy (EDS) confirmed the presence of Mo, S, and W elements at the MoS_2-WS_2 heterojunction, verifying the integration of both MoS_2 and WS_2 through their individual elemental signatures, as depicted in Figure 7.1 (b-d).

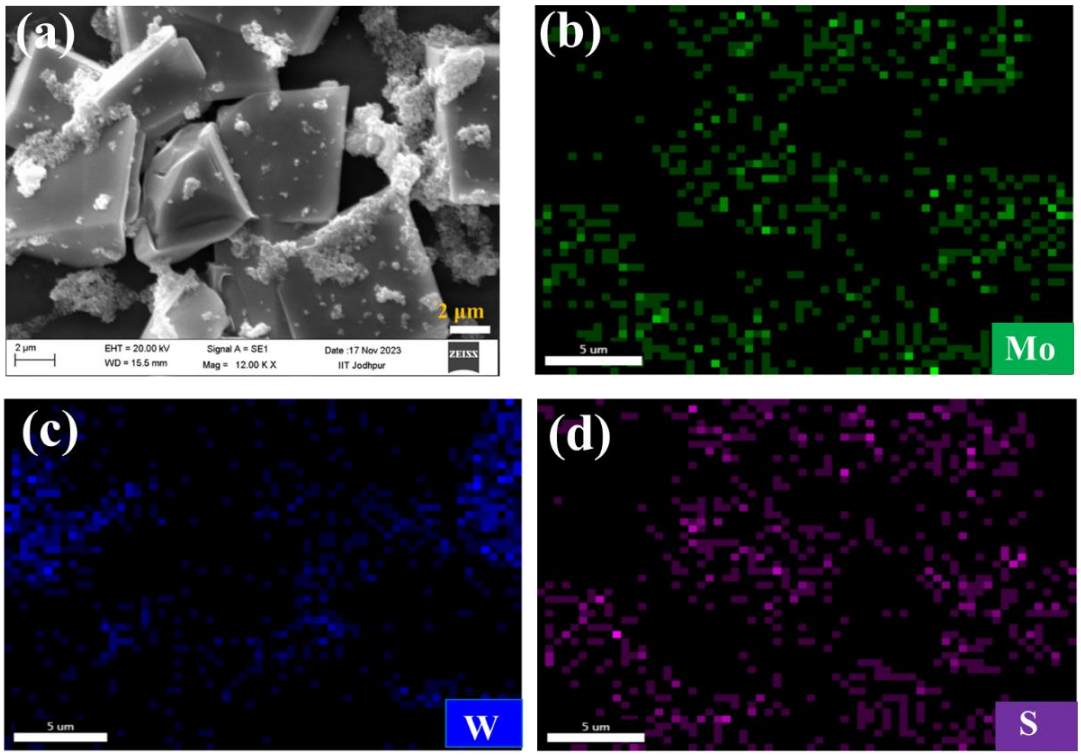

Figure 7.1: (a) FE-SEM image of WS2 nanoparticles decorated MoS_2 flakes network, (b, c, d) EDX element mapping pictures of the MoS_2-WS_2, confirming the existence of Mo, W and S.

We performed Raman measurements in order to confirm the existence of MoS_2, WS_2 and their heterostructure nature using optical phonon modes, as shown in Figure 7.2 (a). There are two prominent peaks in the Raman spectra of pristine MoS_2 at ~ 383 cm^{-1} and ~ 408 cm^{-1}, with respect to in-plane vibration mode (E^1_{2g}) of both S and Mo in the opposite direction and out-of-plane vibration mode (A_{1g}) of only Mo with fixed S in opposite direction, respectively [Kumar et al., 2017; Lee et al., 2010]. We observe that pure WS_2 has two Raman peaks, at 353 cm^{-1} (E^1_{2g}) and 416 cm^{-1} (A_{1g}), respectively [Zhang et al., 2018d]. As demonstrated in Figure 1b, the presence of both materials and the development of a MoS_2-WS_2 heterojunction are confirmed by the signature of four Raman characteristic peaks positioned at 350 cm^{-1}, 382 cm^{-1}, 408 cm^{-1}, and 417 cm^{-1} corresponding to each material WS_2 (E^1_{2g}), MoS_2 (E^1_{2g}), MoS_2 (A_{1g}), and WS_2 (A_{1g}), respectively. Figure 7.2 (b), shows the PL spectra of pristine MoS_2, WS_2, and MoS_2-WS_2 heterostructure using a focused excitation laser (532 nm). The MoS_2 films have a binding energy of PL peak at 1.84 eV

(red curve), corresponding to 674 nm. In addition, the A-exciton emission peak of single-layer WS_2 occurs at a wavelength of 626 nm, with a PL peak location of 1.98 eV [Chen et al., 2016]. The MoS_2 peak moves marginally to 1.84 eV in the MoS_2-WS_2 heterostructure, whereas the WS_2 peak moves slightly to 1.98 eV, both relative to their respective bulk peaks. Interlayer coupling between two layers is responsible for these energy changes, and the average coupling strength is found to be 0.045 eV [Han et al., 2020; Hong et al., 2014].

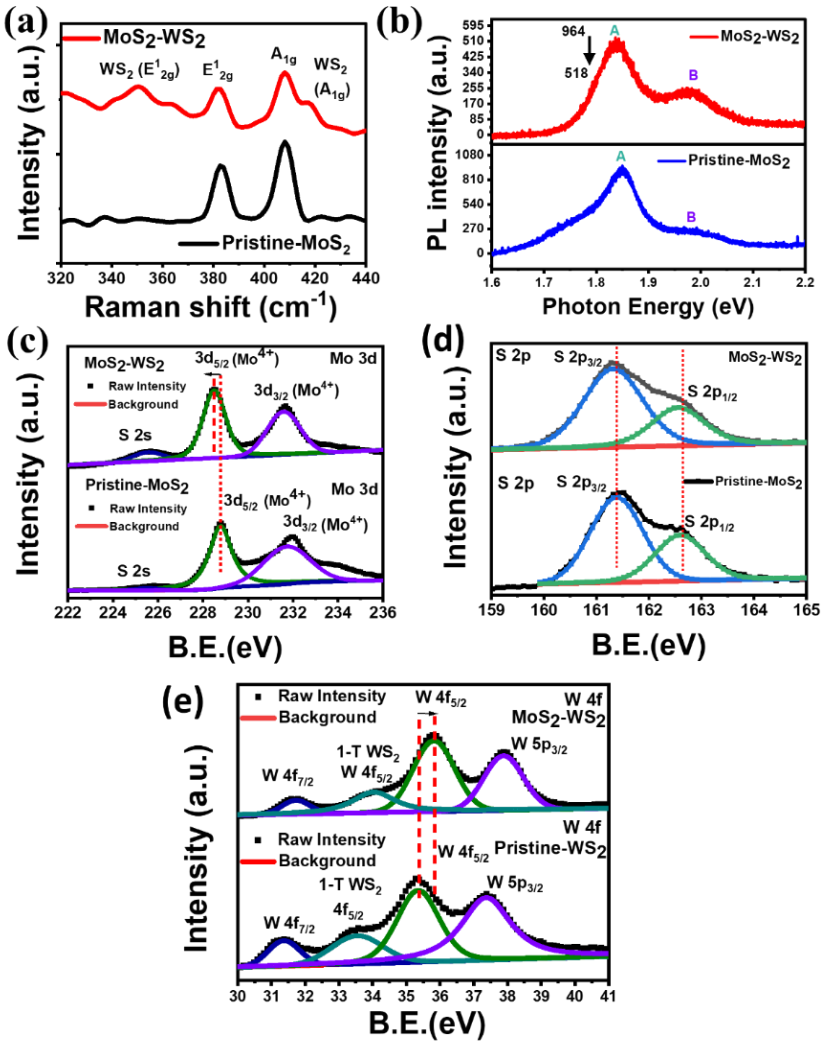

Figure 7.2: (a) Raman spectrum of pristine-MoS_2 and MoS_2-WS_2 heterostructures (b) PL spectra of pristine-MoS_2 and MoS_2-WS_2 heterostructures. XPS spectra of pristine-MoS_2 and MoS_2-WS_2 heterostructures (c) Mo 3d, (d) S 2p, and (e) W 4f peaks, respectively.

XPS spectroscopy was used to determine the Chemical states and surface composition of the MoS_2 that had been adorned with WS_2. Figure 7.2 (c-e), shows high-resolution core level spectra of Mo 3d, S 2p, and W 4f for MoS_2-WS_2 heterostructure and pristine MoS_2 respectively. The deconvolution peaks at 228.82, 228.48 and 231.72, 231.58 eV are related to Mo $3d_{5/2}$ and Mo $3d_{3/2}$ corresponding to pristine MoS_2 and MoS_2-WS_2 heterostructure, respectively. Also, the curve indicates that Mo peaks at 233.88 eV and 234.32 eV, corresponding to Mo^{+6} state due to presence molybdenum oxides sample after CVD development and post-synthesis exposure to air [Xue et al., 2016]. Figure 7.2 (d), depicts the binding energy peaks for the S $2p_{3/2}$ and S $2p_{1/2}$ states at 161.41and 162.58 eV, respectively. Figure 7.2 (e), depicts the W 4f spectra having 1T-and 2H-WS_2 phase and 2H-WS_2 deconvoluted into two peaks located at 31.39, and 35.30 eV, which belong to W $4f_{7/2}$, and W $4f_{5/2}$, respectively. The observed peak positions and shape of W 4f and Mo 3d indicate the coexistence of WS_2 and MoS_2, as reported in the literature [Lonkar et al., 2020]. At the MoS_2-WS_2 heterostructure, it was found that a change in the binding energy of the Mo 3d core levels had occurred after detailed examination of the XPS core-level energy spectrum. Mo $3d_{5/2}$

and Mo $3d_{3/2}$ peak location had a redshift of 0.234 and 0.14 eV level spectra indicates combined actions of the inherently n-type TMDCs, MoS_2 and WS_2 both have a negative net charge within the heterostructure [Chiu et al., 2017]. This change in core-level spectra immediately points to interlayer interaction and transfer of charge between MoS_2 and WS_2.

7.4 Effects of visible to near-infrared wavelength on the MoS_2-WS_2 heterojunctions

We fabricated pristine-MoS_2 and WS_2 decorated on the MoS_2 sample to evaluate the photodetector performance parameters with a voltage biasing range of ±5V, as seen in Figure 7.3 (a). Figure 7.3 (b), depicts the current-voltage (*I-V*) behavior of pristine MoS_2 and MoS_2-WS_2 heterostructure photodetector in the dark condition. The photoresponse of a MoS_2-WS_2 heterostructure was studied by using a different volume of drop-cast WS_2 solution (1µl-20 µl). We find that the photoresponse of the heterostructure improves with increasing WS_2 concentration up to a saturation point at 10 µl. However, the photocurrent begins to decrease when the number of WS_2 NPs surpasses 10µl, indicating that this concentration is the optimum amount of WS_2 at the heterointerface for optimal device performance. The *I-V* characteristics of pristine MoS_2 photodetector in dark and exposure of Visible-NIR spectrum is depicted in Figure 7.3 (c). Figure 7.3 (d), depicts the current-voltage (*I-V*) behaviour of MoS_2-WS_2 heterostructure photodetector in the dark condition and under the illumination of different wavelength from visible to NIR domain (405-800 nm). The *I-V* curve shows that the MoS_2-WS_2 heterostructure displayed a significant rise in photocurrent in the Visible to NIR range, whereas the photo response of pristine MoS_2 showed only a small increase in current upon exposure to light (visible-NIR) as compared to its dark current. MoS_2-WS_2 heterostructure has an improved broadband photoresponse as a result of greater absorption in the Visible-NIR region and a significant built-in potential at the interface. Furthermore, we observe that the photocurrent created by the 580 nm light is higher than that of the other wavelength, which is due to the high photon energy. In addition, the comparison of the photocurrent of 10 µl solution-based WS_2-MoS_2 and pristine MoS_2 at 580nm of light, is mentioned in Figure 7.3 (e, f). It is observed that the current conduction behaviour was significantly affected by the decoration of WS_2 as compared to the pristine MoS_2 flakes.

In order to determine the performance of the device, we determined the self-powered photodetector's figures of merit, such as responsivity (R), external quantum efficiency (EQE), and detectivity (D*). One of the most important characteristics of a photodetector is its responsivity (R), which is defined as the ratio of the generated photocurrent to the incident optical power, can be written as equation 7.1[Lei et al., 2021]:

$$R = \frac{I_{Photo} - I_{dark}}{P_{in} \,.\, A} \quad (A/W) \tag{7.1}$$

Where, I_{Photo} and I_{dark} are photocurrent, and dark current P_{in} is the optical power density of the incident light source, and A is an effective area of the device (0.0091 cm^2), respectively.

Figure 7.4 (a), shows the responsivity of pristine MoS_2, and MoS_2-WS_2 heterojunction under Visible-NIR (405-800 nm) light at zero bias voltage (0V). The MoS_2-WS_2 heterojunction exhibits a high responsivity (R=282.77 mA/W), 12 times higher than pristine MoS_2 (R=23.55 mA/W), under illumination of 580 nm light. Further, assuming that the shot noise is dominated by a dark current, we determined the specific detectivity (D*) of the fabricated photodetector, which determines the ability of the photodetector to detect the weak optical signal and is given by the following equation 3 [He et al., 2021]:

$$D^* = \frac{R.\sqrt{A}}{\sqrt{2q.I_{dark}}} \tag{7.2}$$

Where A represents an active area of the device, R is responsivity, q is the electron charge and I_{dark} is the dark current of the device. According to equation (7.2), we calculated the specific detectivity

(D*) of pristine MoS_2 and MoS_2-WS_2 heterostructure self-power photodetector (0V) under irradiation of different wavelength, as shown in Figure 7.4 (b).

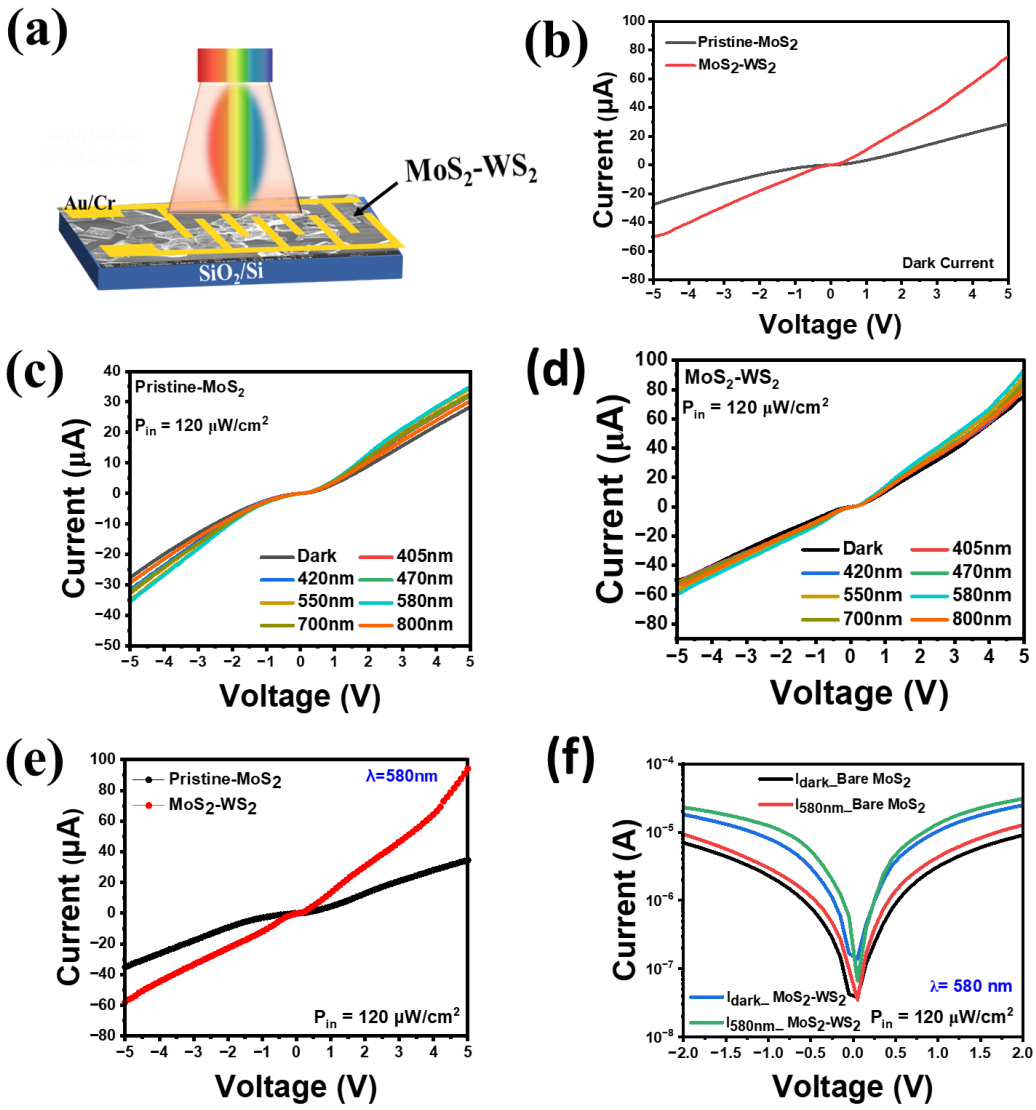

Figure 7.3: Self-powered Electrical characterizations and photoresponse characteristics MoS_2-WS_2 heterostructure devices. (a) Schematic of the device. Current-voltage (*I-V*) characteristics measured in the dark and under different wavelengths. (b) Dark current, (c) Pristine-MoS_2, (d) MoS_2-WS_2 heterostructure, (e) *I–V* curves of the pristine-MoS_2 and MoS_2-WS_2 heterojunction under light illumination (580 nm, 120 μW/cm^2), and (f) Comparison of semi-logirthm *I-V* of Pristine MoS_2 and MoS_2-WS_2 in the dark condition and light illumination (580 nm, 120 μW/cm^2).

The MoS_2-WS_2 heterostructure predicted detectivity is in the range of 10^{12} Jones, which is significantly higher than the pristine MoS_2 photodetector (10^{11} Jones). At 580nm the MoS_2-WS_2 heterostructure-based photodetector has a maximum D*, which suggests that the visible region has a greater capacity for the detection of weak optical signals. Also, the photo-conversion efficiency of the device, known as EQE, is determined using the following mathematical equation 7.3[Xie et al., 2017a].

$$EQE = \frac{Rhc}{q.\lambda} \; x \; 100\% \qquad (7.3)$$

Here R, h, c, q, and λ are the responsivity, Planck's constant, speed of light, electron charge, and wavelength of incident optical light, respectively. Figure 7.4 (c), shows an EQE study of a self-powered photodetector performed under a broad spectral range for both the MoS_2-WS_2 heterostructure and pristine MoS_2 devices. Under 580 nm illumination, the computed EQE for the

MoS_2-WS_2 heterostructure and for pristine MoS_2 are 60.59 % and 5.01 %, respectively. The MoS_2-WS_2 heterostructure's EQE is 12 times more than pristine MoS_2.

Further, the performance of the self-power photodetector, including its detectivity and responsivity, is examined under the irradiation of 580 nm light with a power density ranging from 3 μW/cm²to 417 μW/cm². We can see that responsivity (R) and specific detectivity (D*), decreases monotonically as laser power increases, indicating a strong relationship with power intensity, as depicted in Figure 7.4 (d, e). This improvement is attributed to interlayer coupling and charge transfer of the heterojunction from the valence band to the conduction band in the MoS_2-WS_2 is caused by the increased number of incoming photons with rising power density. The MoS_2-WS_2 heterostructure predicted detectivity is in the range of 10^{12} Jones, which is significantly higher than the pristine MoS_2 photodetector (10^{11} Jones), as shown in Figure 4b. At 580nm the MoS_2-WS_2 heterostructure-based photodetector has a maximum D*, which suggests that the visible region has a greater capacity for the detection of weak optical signals. We also measured the MoS_2-WS_2 heterostructure photodetector performance parameters R, as a function of bias voltage under 580 nm light are depicted in Figure 7.4 (f). The photodetector exhibits the *R* 7.37 A/W, at an applied bias voltage of 5 V under 580 nm light source illumination.

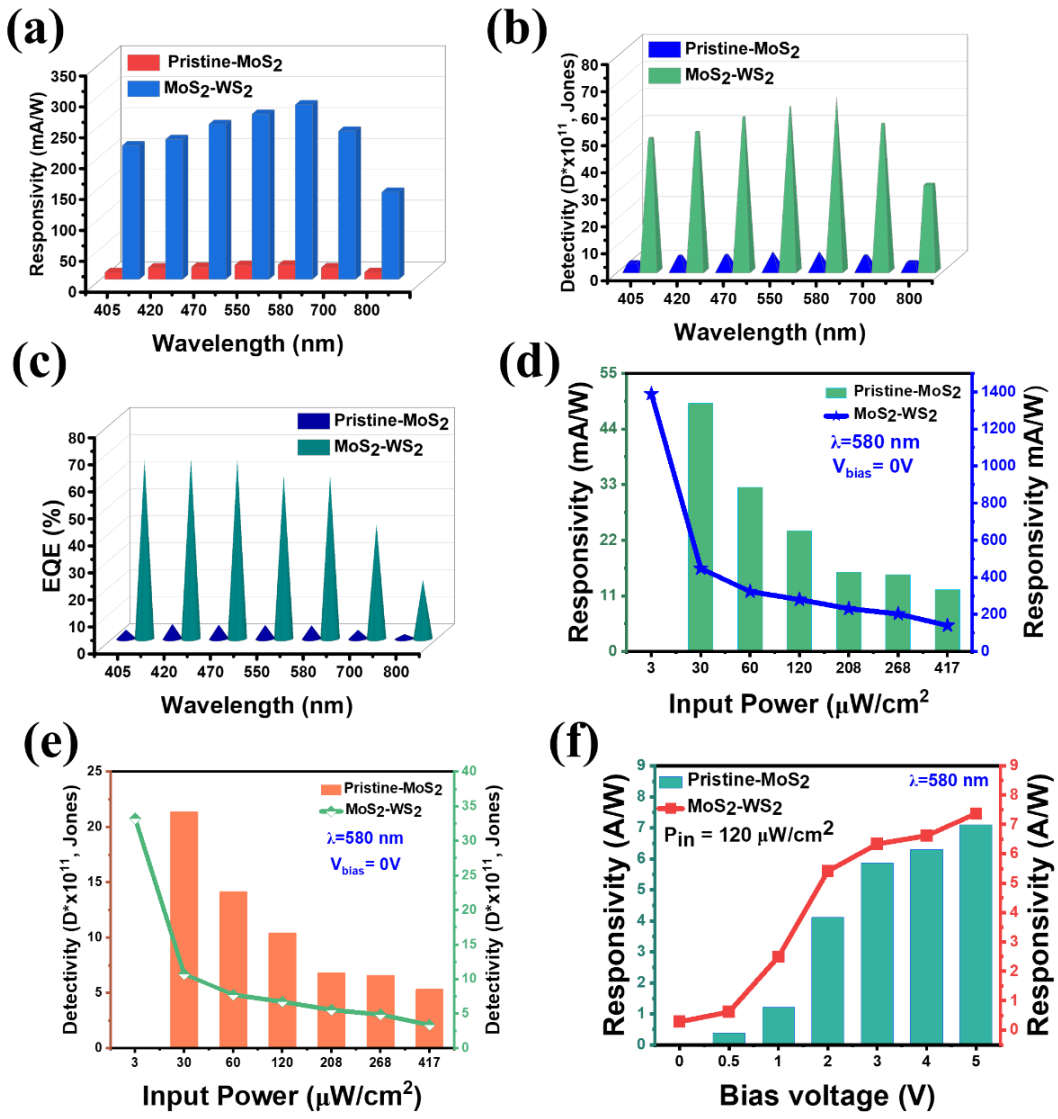

Figure 7.4: Photoresponse characteristics of self-powered device. (a) Responsivity, (b) Detectivity, (c) EQE of pristine MoS_2 and MoS_2-WS_2 under irradiation of Visible-NIR spectrum, respectively with an input power density (P_{in}) of 120 μW/cm², (d, e) Responsivity and Detectivity with function of different incident optical power density, and (f) Comparison of Responsivity of pristine MoS_2 and MoS_2-WS_2 under light illumination of 580nm with various bias voltages.

The transient photoresponse of the pristine MoS_2 and MoS_2-WS_2 heterostructure devices in self-powered mode was investigated in the wavelength range of 405 to 800 nm with repeatedly switching on/off in cycles of 30 s at a power density of 120 μW/cm², as depicted in Figure 7.5 (a, b). In order to understand the photoresponse stability of the pristine MoS_2 and MoS_2-WS_2 heterostructure-based photodetector for real-world use, the dynamic photocurrent response is examined by controlling the incident light intensity and applied bias voltage. The pristine MoS_2 and MoS_2-WS_2 heterostructure-based photodetector dynamic photocurrent response at various power densities, when repeatedly turned on and off the light of 580nm is shown in Figure 7.5 (c, d). As shown in Figure 7.5 (e, f), the time-related current of the pristine MoS_2 and MoS_2-WS_2 device is also measured at various positive bias voltages V_{bias}, while illuminated by a 580 nm (120 μW/cm²) light. We also It shows that the photocurrent of device increased with an increase in bias voltage. This is due to the thermionic field emission being proportional to the applied bias voltage i.e., an increase in bias voltage increases thermionic emission.

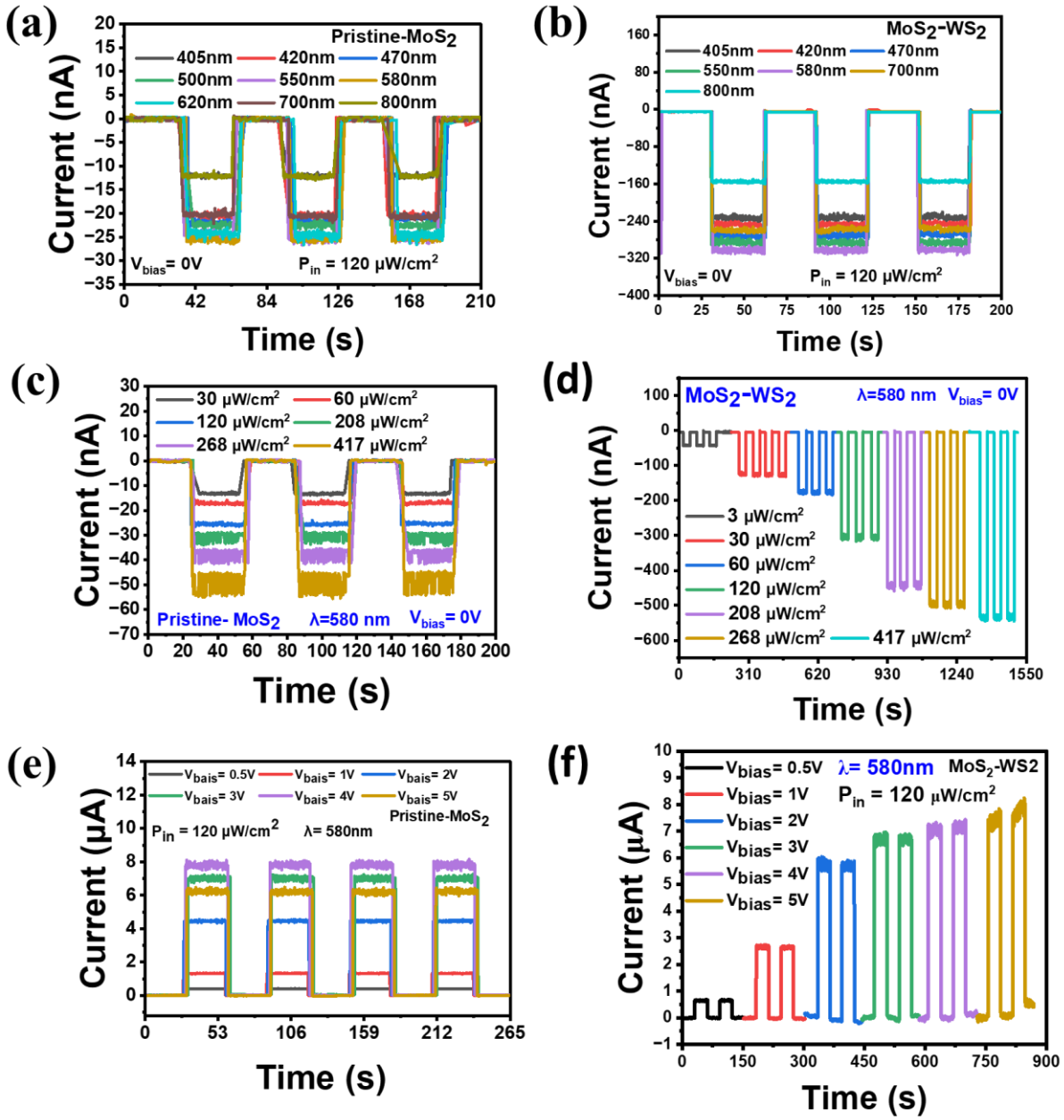

Figure 7.5: Comparative transient of pristine MoS_2 and MoS_2-WS_2 heterostructure with (a, b) Wavelength-dependent photoresponse, (c, d) different incident optical power density, and (e, f) Transient photoresponse measurement at different bias voltage at 580 nm wavelength of light at an incident optical power of 120 μW/cm².

7.5 Speed and stability of the photodetector

The device's performance is strongly reliant on its rise and fall times i.e., response speed. Therefore, we determine the response speed of the MoS_2-WS_2 heterostructure and pristine MoS_2 devices by fitting the temporal photo response of 580 nm light with the incident power of 120 $\mu W/cm^2$ as shown in Figure 7.6 (a, b). We can see that the rise/fall time of the MoS_2-WS_2 heterostructure is ~375µs/6ms and 7.2 ms/10.8 ms in case of pristine MoS_2 at 0 V under irradiation of 580 nm wavelength of light. Furthermore, for all incident visible-NIR light, rapid optical switching with low response speed (on the order of microsecond) has been seen in heterojunction. Due to the strong suppression of carrier recombination and effective carrier transportation at the interface of the MoS_2-WS_2 heterostructure, the photoresponse behaviour of the proposed heterostructure is greatly enhanced by the introduction of faster charge transport. Table 7.1 presents a comparison of the self-powered photodetector's figures of merit of MoS_2-WS_2 photodetector with other 2D/2D heterostructure devices. As illustrated in Figure 7.6 (c, d), the self-powered pristine MoS_2 and MoS_2-WS_2 heterostructure devices demonstrated outstanding repeatability and stability after 30 days of re-measuring at 580 nm light.

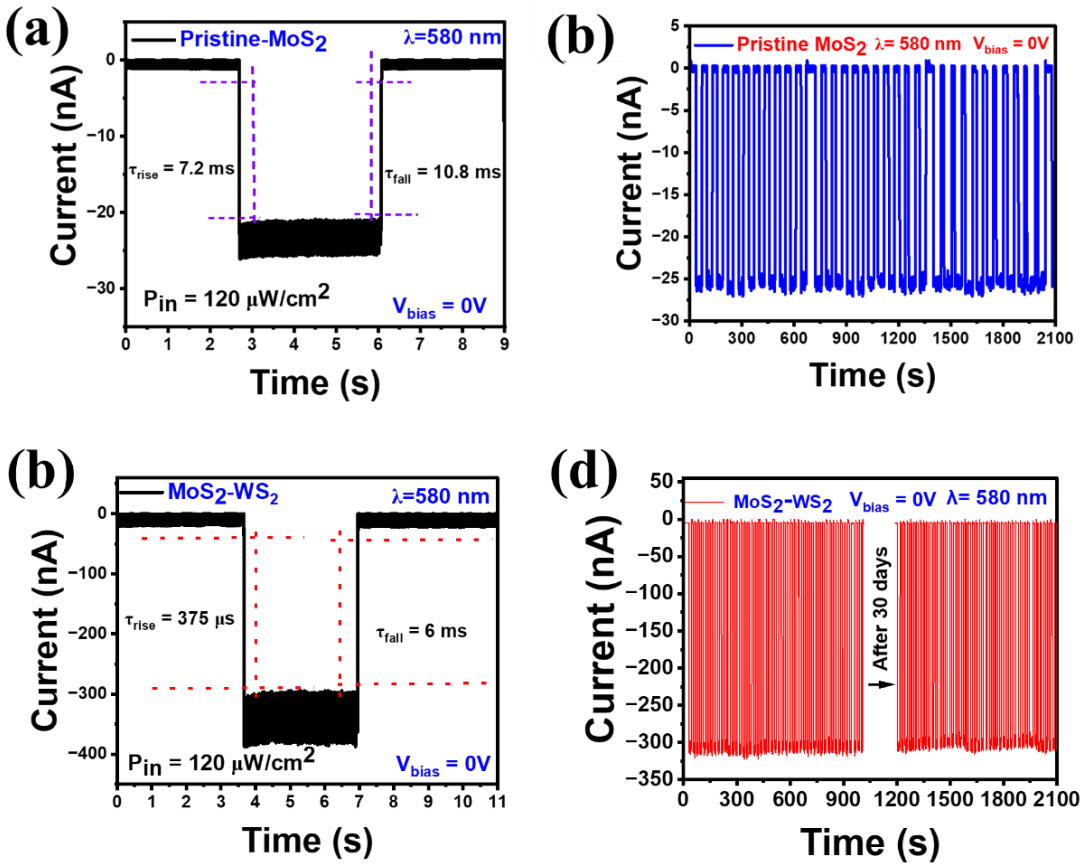

Figure 7.6: Rise time and fall time of (a) Pristine MoS_2, (B) MoS_2-WS_2 heterojunction, and (c, d) Long-term stability of Pristine MoS_2 and MoS_2-WS_2 heterostructure device with 100 cycles under 580 nm light illumination after 30days in ambient air.

Table 7.1: Comparison of self-powered photodetector figure of merit.

photodetectors	Detection range (nm)	Responsivity (AW^{-1})	Detectivity (Jones)	Response time (τ_{rise}/ τ_{fakk}) (ms)	Ref.
MoS_2-ReS_2	400–1100	1.28	1.34 x 10^{13}	30/71	[Wadhwa et al., 2021b]
MoS_2/GeSe	380–1064	0.105	1.03 × 10^{10}	110/750	[Xin et al., 2020]
MoS_2/Ga_2O_3	230–1000	94.92	7.72x 10^9	290/300	[Varshney et al., 2023]
WS_2/SnSe	457-1064	0.099	—	8.2/8.4	[Jia et al., 2016]
MoS_2/$LaVO_3$	300-800	0.14	5 × 10^9	0.3/0.4	[Lee et al., 2023]
nh-MoS_2/WSe_2	532-950	0.177	8 × 10^{10}	33/38	[Sharma et al., 2023]
MoS_2/CuO	400-1200	10	1.8 × 10^{14}	80/80	[Kumawat et al., 2022]
MoS_2/SnO_2	400-1100	0.35	1.25 × 10^{11}	153/200	[Augustine et al., 2022]
Gr/$MoSe_2$	450-900	0.0895	2.24 × 10^{10}	9.6/12.8	[Liu et al., 2019]
MoS_2-WS_2	405-800	0.283	6.44 x 10^{12}	375µs/6	This work

7.6 Self-powered functionality of CVD-synthesized MoS_2 photodetectors

With symmetric Au electrodes, we present a high-performance, self-powered MoS_2 photodetector that differs from the most common self-powered photodetectors based on the asymmetric contact electrodes or heterostructures mentioned above. Strong evidence that the self-powered functionality of CVD-synthesized MoS_2 photodetectors arises from the complex interaction between intrinsic defects, like sulphur vacancies, as well as interactions with environmental factors like temperature and humidity is presented by this comprehensive methodology, which combines electrical characterisation with structural and surface potential analyses[Kaushik et al., 2017; Park et al., 2013; Shu et al., 2016]. A built-in electric field may be generated in symmetric electrode photodetectors by charge trapping, particularly in CVD-grown MoS_2 containing defect states (such as sulphur vacancies)[Kunstmann et al., 2017; Senkić et al., 2023]. Typical flaws in CVD-grown MoS_2 include grain boundaries and vacancies, which can trap charge carriers[Ma et al., 2022]. Additional traps may form at the MoS_2/substrate interface, when grown on insulating substrates such as SiO_2/Si[Liu et al., 2018c]. Charge trapping and detrapping effects can be caused by these flaws' creation of localised energy states. Without the need for an external bias, this intrinsic field can assist in the separation of photogenerated electron-hole pairs, enabling a self-powered reaction when exposed to light. A potential difference across the MoS_2 layer may be created via the charge trapping effect, which changes the threshold voltage and enables the direct collection of photogenerated carriers. These findings are in line with other studies showing that adsorbed species and sulphur vacancies significantly affect charge trapping, hysteresis, and photodetection behaviour in MoS_2-based devices. This behaviour is confirmed by

a combination of Raman mapping, Kelvin Probe Force Microscopy (KPFM) studies, and hysteresis loop occurs in the *I-V* characteristics.

Hysteresis in *I-V* measurements performed in dark conditions at different voltage scan rates highlights the critical importance of surface charge changes, when the voltage is swept in one direction and does not quickly release when the sweep is reversed. Charge trapping and de-trapping processes enabled by defect states (such as sulphur vacancies) and adsorbed molecular entities on the MoS_2 surface cause a discernible hysteresis at reduced scan rate. At high scan speeds, these effects decrease because trapped charges do not have enough time to respond, which results in less hysteresis. The remarkable association between scan rate and hysteresis suggests that surface charges caused by adsorbed ambient species and sulphur vacancies play a significant role in the observed phenomena. Both internal and extrinsic factors have been implicated in the sustained photoconductivity observed in MoS_2 photodetector. Photocharge trapping in localised band-tail states of MoS_2 is the inherent effect [Di Bartolomeo et al., 2017; Furchi et al., 2014], whereas photocharge trapping in residues and adsorbates deposited on the top or bottom MoS_2 surface is an extrinsic cause. Trap states can be produced by dangling bonds in the underlying dielectric, whereas adsorbed oxygen and moisture molecules or processing residues are the primary causes of top trap states[Cho et al., 2014; Wu et al., 2015]. In the *I-V* characteristics of MoS_2, hysteresis is a phenomenon associated with persistent photoconductivity, which is also associated with charge transfer/trapping. The *I-V* characteristics in a sequence of voltage scan rates are displayed in Figure 7.7. The trap center, which might be on the surface of the channel material or at the interface between the dielectric surface and the channel material, is typically responsible for hysteresis, according to the study. It was reported that the hysteresis in MoS_2 transistors is caused by (i) the interfacial trap states between MoS_2 and the SiO_2 substrate and (ii) the sulphur vacancy, which serves as both the trap centre and a facilitator of external molecular adsorption, both of which increase the hysteresis performance[Late et al., 2012; Prasad et al., 2020; Urban et al., 2019]. However, it was subsequently shown that hysteresis is still present in a suspended MoS_2 transistor; the hysteresis is stronger in a thinner MoS_2 than in a thicker MoS_2, suggesting that the inherent sulphur vacancy in MoS_2 transistors is the source of the hysteresis[Shu et al., 2016]. Due to inherent flaws in the MoS_2 lattice and the interfacial trap at the MoS_2/SiO_2 contact, the present trap states are highly likely[Liu et al., 2018c]. Therefore, we suggest that the sulfur-vacancy-dominant hysteresis behaviour, which differs from that of the interfacial oxygen functional group at the MoS_2/SiO_2 interface, may be the origin of the current unexpected hysteresis behaviour.

When combined with the electrical evaluations, Raman mapping provides detailed structural information. It clarifies the spatial differences between the vibrational modes E^1_{2g} and A_{1g}, which frequently undergo broadenings or shifts due to defects such as sulfur vacancies. Different colour contrasts were seen in the mapping of the E^1_{2g} and A_{1g} mode intensities, which corresponded to areas with varying concentrations of defects and strain, as shown in Figure 7.8 (a-d).These defects may be caused by substrate contacts or uneven growth conditions during CVD. Grain boundaries and sulphur vacancies, which are known to cause local disorder and impact the material's vibrational modes, frequently occurred with areas of high defect density and extreme colour contrast in the Raman maps. These features, which are known to impact charge dynamics and electrical properties inside MoS_2, provide unmistakable proof of structural defects. We also used Kelvin Probe Force Microscopy (KPFM) to investigate the distribution of surface charges on pristine MoS_2, as seen in Figure 7.8 (e-f). The surface potential difference, which represents the local differences in the work function caused by defects, doping, or surface charges, may be quantitatively mapped using KPFM [Yim et al., 2022]. Areas of increased surface potential correlating to regions identified as defect or strained using Raman mapping were corroborated by the surface potential mapping acquired through KPFM, which revealed the presence of localised charge heterogeneities throughout the MoS_2. The presence of defects, such sulphur vacancies or edge states, can lead to charge redistribution and changes in the local electronic structure of the material. This can be seen in variations in surface potential. These inherent fields

are essential for encouraging charge separation under light, which makes self-powered photodetection possible.

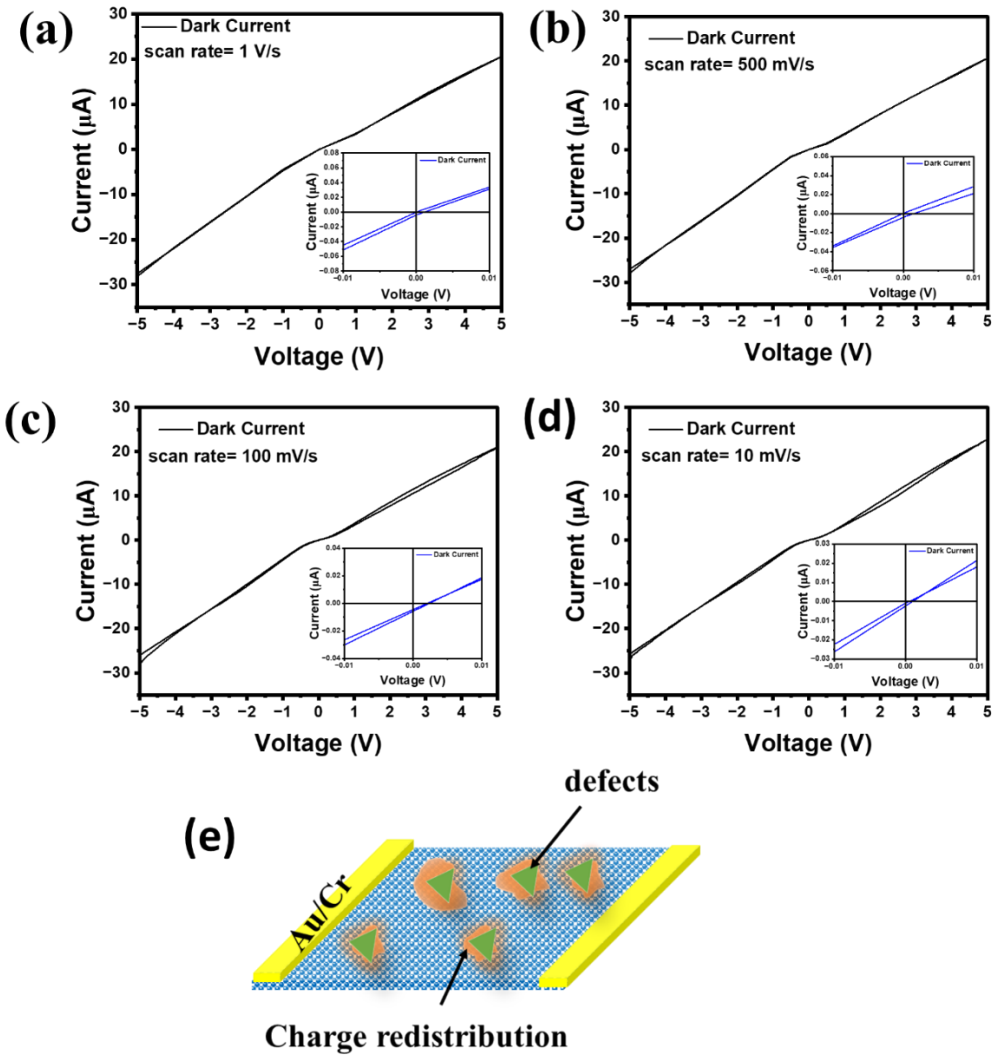

Figure 7.7.: Hysteresis behavior of I–V as a function of different sweeping rates (a) 1V/s, (b) 500 mV/s, (c) 100 mV/s, (d) 10 mV/s, with inset graph showing the magnified I-V of device, and (e) Schematic of the defects generate charge redistribution in pristine MoS2.

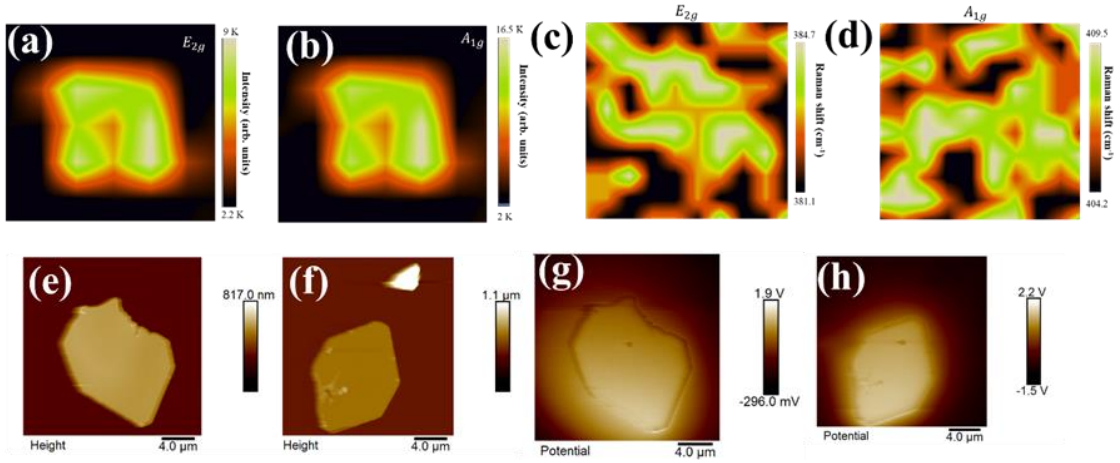

Figure 7.8: Raman mapping of Pristine MoS2 (a, b) position mapping shows clear intensity difference between E2g and A1g mode, (c, d) and KPFM study of Pristine MoS2 (e-f) mapping of variation in thickness, (g, h) Surface potential images for pristine-MoS2

7.7 Light sensing mechanism of the photodetector

For effective data transfer in high-speed optical communication and other sophisticated applications, high-frequency detection is necessary for fast decoding of optical signals. Significant applications include LIDAR and imaging systems, where it improves resolution and accuracy, time-resolved spectroscopy, which records quick transient events and dynamic processes, and so on. Hence, we investigated the device's frequency-dependent transient current (I-T) response throughout a wide frequency range (1 Hz to 1 kHz) using optical chopper, to execute the modulation of light with varying frequencies. Figure 7.9 (a), displays the schematic diagram illustrating the measuring process. Figure 7.9 (b-d), illustrates the typical temporal response characteristics of the heterojunction photodiode at a frequency of 1 Hz, 100 Hz, and 1 kHz, indicating the potential for high frequency photodetection, when subjected to a reverse bias of 1 V. With no indications of performance deterioration or cut-offs, the gadget continued to display outstanding repeatability even at the higher frequency of 1 kHz.

We have provided an in-depth understanding of the formation and motion of charge transfer at the interface between WS_2 and MoS_2 under the influence of light irradiation at various wavelengths. This was achieved by the use of an energy band diagram of the heterostructure, which demonstrates its self-powered behaviour under equilibrium conditions, as illustrated in Figure 7.9 (e). The stacking of MoS_2-WS_2 semiconductors facilitates the creation of high-quality heterostructures, without imposing limitations on lattice misfit. The photoconductive effect occurs when a single semiconductor material is exposed to visible-NIR radiation (at so). The electrons in the valence band (VB) absorb the photon's energy and migrate to the conduction band (CB) to create electron-hole pairs, increasing conductivity. However, a type II band alignment structure is created, when MoS_2 and WS_2 samples are combined to produce heterostructures, as seen in Figure 6f [Gong et al., 2014; Lin et al., 2021]. Electrons and holes would separate into different layers in order to achieve equilibrium, and electrons in the conduction band would be transferred from WS_2 to MoS_2 and the holes in the valence band would be transferred from MoS_2 to WS_2, resulting in n-doping and p-doping for MoS_2 and WS_2 respectively, as shown in Figure 7.9 (f). The passivated MoS_2 layer prevents surface leakage current, and the built-in electric field enables this device to operate at zero bias voltage. Photogeneration of electron-hole pairs takes place in the heterostructure when it is subjected to visible (Vis) light with an energy that is equivalent to or greater than its bandgap energy [Qin et al., 2022]. MoS_2 has the ability to absorb light in both the visible (Vis) and near-infrared (NIR) regions of the electromagnetic spectrum, resulting in the generation of electron-hole pairs. The presence of local electric fields at the interface between WS_2 and MoS_2 inhibits the recombination of photogenerated electrons from MoS_2 under the exposure of visible (Vis) or near-infrared (NIR) light [Lu et al., 2019]. The enhancement of charge separation resulting from the electric field developed at the interface between WS_2 and MoS_2 is attributed to the role of WS_2 in the detection of visible (Vis) and near-infrared (NIR) light. This is equivalent to increasing the conductance of the MoS_2 and WS_2 channels simultaneously, resulting in a larger photocurrent.

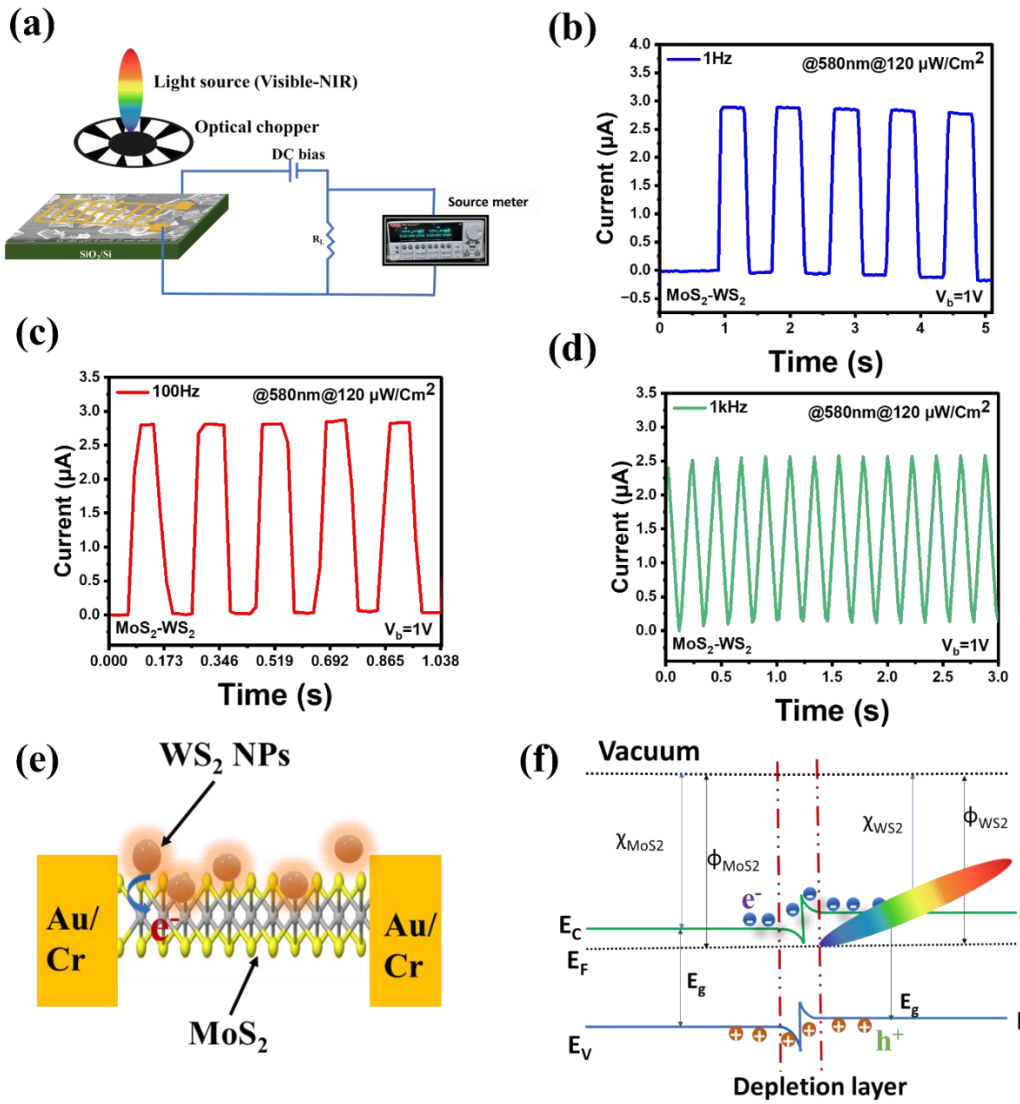

Figure 7.9: (a) Schematic illustration of the measurement configuration for the modulation of light, and (b-d) Representative photoresponse of the heterojunction photodiode under 580 nm light illumination with the modulated chopper frequency of 1 Hz, 100 Hz, and 1kHz respectively, Band alignment and charge transfer at the heterostructures. (e) a sketch of WS2 particle-decorated on MoS2-based photodetector, and (f) Schematic of Band profiles of MoS2 and WS2, which forms a type II heterojunction relative to the vacuum level.

7.8 Summary

In summary, self-powered photodetectors based on the MoS_2-WS_2 heterostructure were successfully fabricated by decorating WS_2 onto MoS_2 films grown using chemical vapour deposition (CVD) techniques. The surface morphology and structural features of the MoS_2-WS_2 heterojunctions were assessed using several analytical techniques, including XPS, Raman spectroscopy, FESEM and photoluminescence spectroscopy. By leveraging the effective interlayer charge transfer mechanism between WS_2 and MoS_2, the MoS_2-WS_2 device demonstrates a notable photoresponsivity of 282.77 mA/W and a specific detectivity of 6.44 x 10^{12} Jones. Additionally, the device exhibits a response time of ~375μs/6ms, which represents a significant improvement in photoresponsivity compared to the pristine MoS_2 and WS_2 devices. Moreover, anchored WS_2 with MoS_2 may pave the way towards the development of high-performance practical optoelectronic devices due to exceptional stability, high response and dependability in response to visible-NIR radiation in the air.